Supplementary Information for
No major increase in erosion rates in Central Himalayas during the late Cenozoic, revealed by 10Be in the newly dated Valmiki Siwalik section.
Lenard et al.

This supplementary information is organized in three parts: S1. Supplementary Figures, S2. Supplementary tables and S3. Extended methods.

S1. Supplementary figure captions

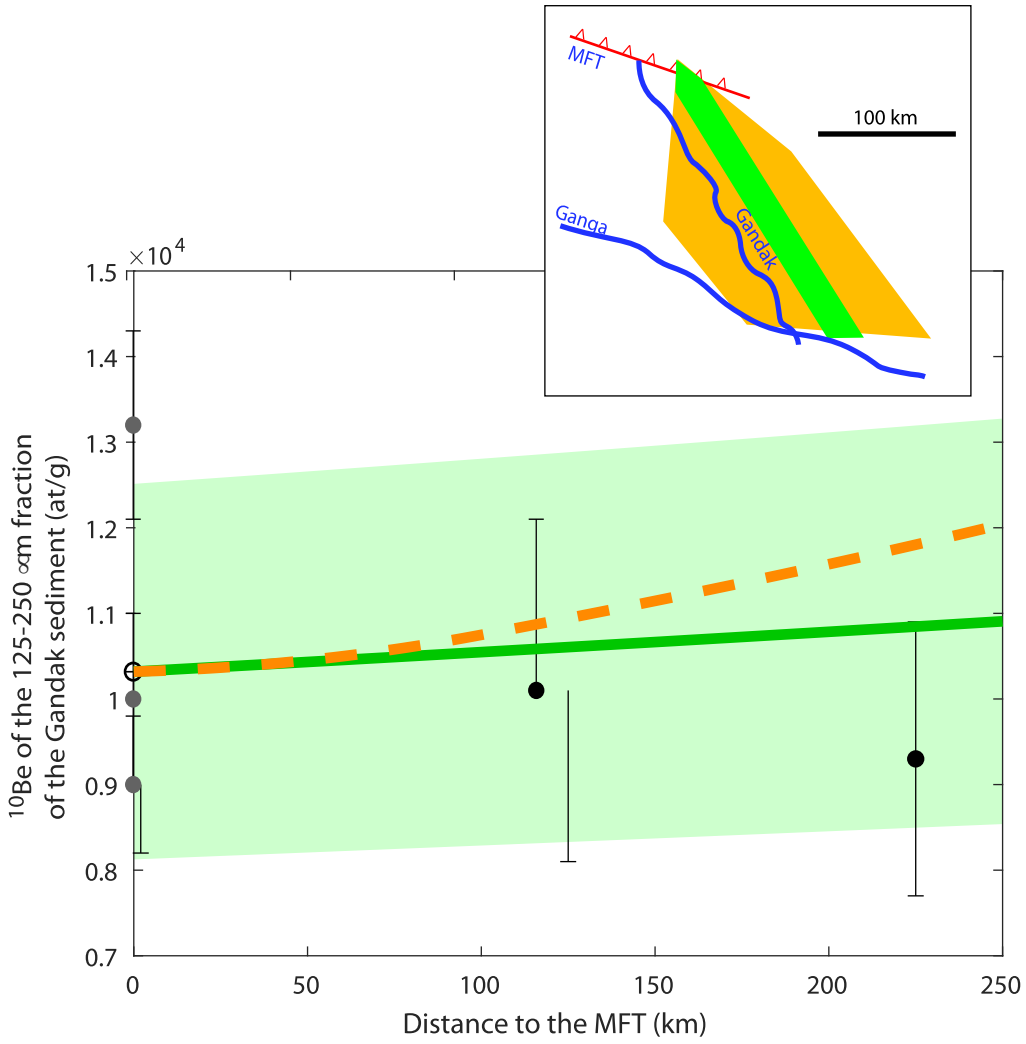

Fig. S1. Validation of the model of 10Be correction for sediment transfer. For modern times, we consider the active fan visited by the Narayani River since ~1ky (Pati et al., 2011) (green surface on the inset map, and green curve with its uncertainty in green shading on the main chart), with comparison to modern 10Be concentrations (Lupker et al., 2012a) at several sites along the river channel. For Siwalik samples, we assume that the river has been visiting a megafan as large as the one aggraded since mid-Holocene time (Pati et al., 2011) (orange surface on the inset map, and orange dashed curve on the main chart). The correction for transfer was calculated using (Lauer and Willenbring, 2010)'s model and the paleo-distance to the topographic front (Fig. 16) and after final deposition using the stratigraphic position of each sample below the top of the sedimentary unit in which we collected it.

Fig. S2. Left bank of the Dwarda River close to the fold frontal part. The location was photographed in November 2012 (a) and May 2016 (b). Bank erosion has modified the bedrock below the strath terrace and its alluvial cover in only three monsoonal seasons. Letters in circle indicate benchmarks. Sites of clayey samples for magnetostratigraphy D117, D119, D121, and sandy samples Dwcos50 and Dwcos51 for isotopic analyses are shown. We collected these samples below cliffs of several meters to minimize recent exposure

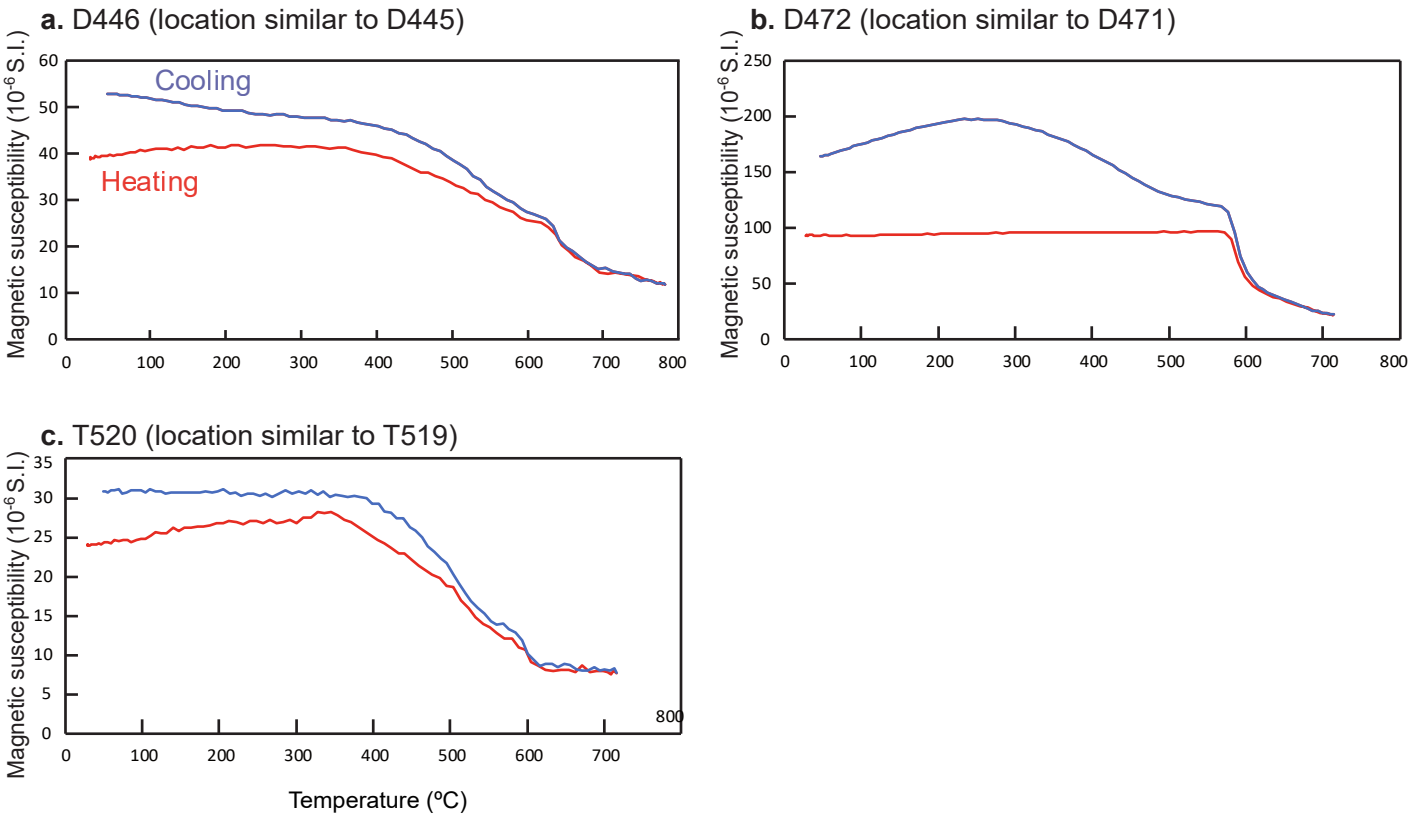

Fig. S3. Thermo-magnetic curves. We measured the curves for each paleomagnetic sample to determine the Curie point. a. and b. Dwarda samples, c. Patalaia sample.

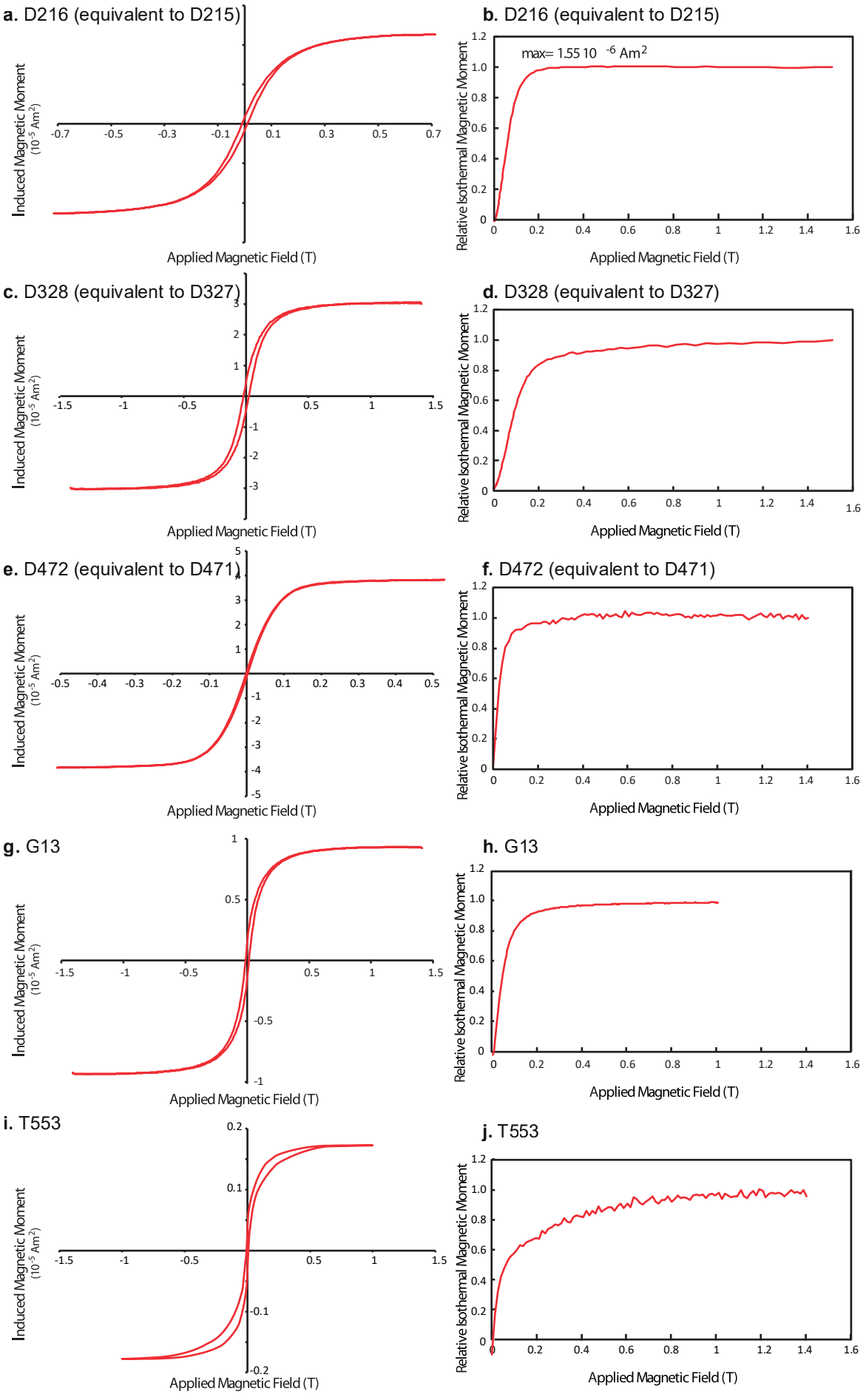
a. D216 (equivalent to D215)
Induced Magnetic Moment (10⁻⁵ Am²)
Applied Magnetic Field (T)
b. D216 (equivalent to D215)
max= 1.55 10 -6 Am2
Relative Isothermal Magnetic Moment
Applied Magnetic Field (T)
c. D328 (equivalent to D327)
Induced Magnetic Moment (10⁻⁵ Am²)
Applied Magnetic Field (T)
d. D328 (equivalent to D327)
Relative Isothermal Magnetic Moment
Applied Magnetic Field (T)
e. D472 (equivalent to D471)
Induced Magnetic Moment (10⁻⁵ Am²)
Applied Magnetic Field (T)
f. D472 (equivalent to D471)
Relative Isothermal Magnetic Moment
Applied Magnetic Field (T)
g. G13
Induced Magnetic Moment (10⁻⁵ Am²)
Applied Magnetic Field (T)
h. G13
Relative Isothermal Magnetic Moment
Applied Magnetic Field (T)
i. T553
Induced Magnetic Moment (10⁻⁵ Am²)
Applied Magnetic Field (T)
j. T553
Relative Isothermal Magnetic Moment
Applied Magnetic Field (T)

Fig. S4. Hysteresis loops (a, c, e, g, i) and Isothermal Remanent Magnetization analyses (b, d, f, h, j). Paleomagnetic samples are shown for the Dwarda (a-f), for the Ganguli (g-h) and the Patalaia (i-j).

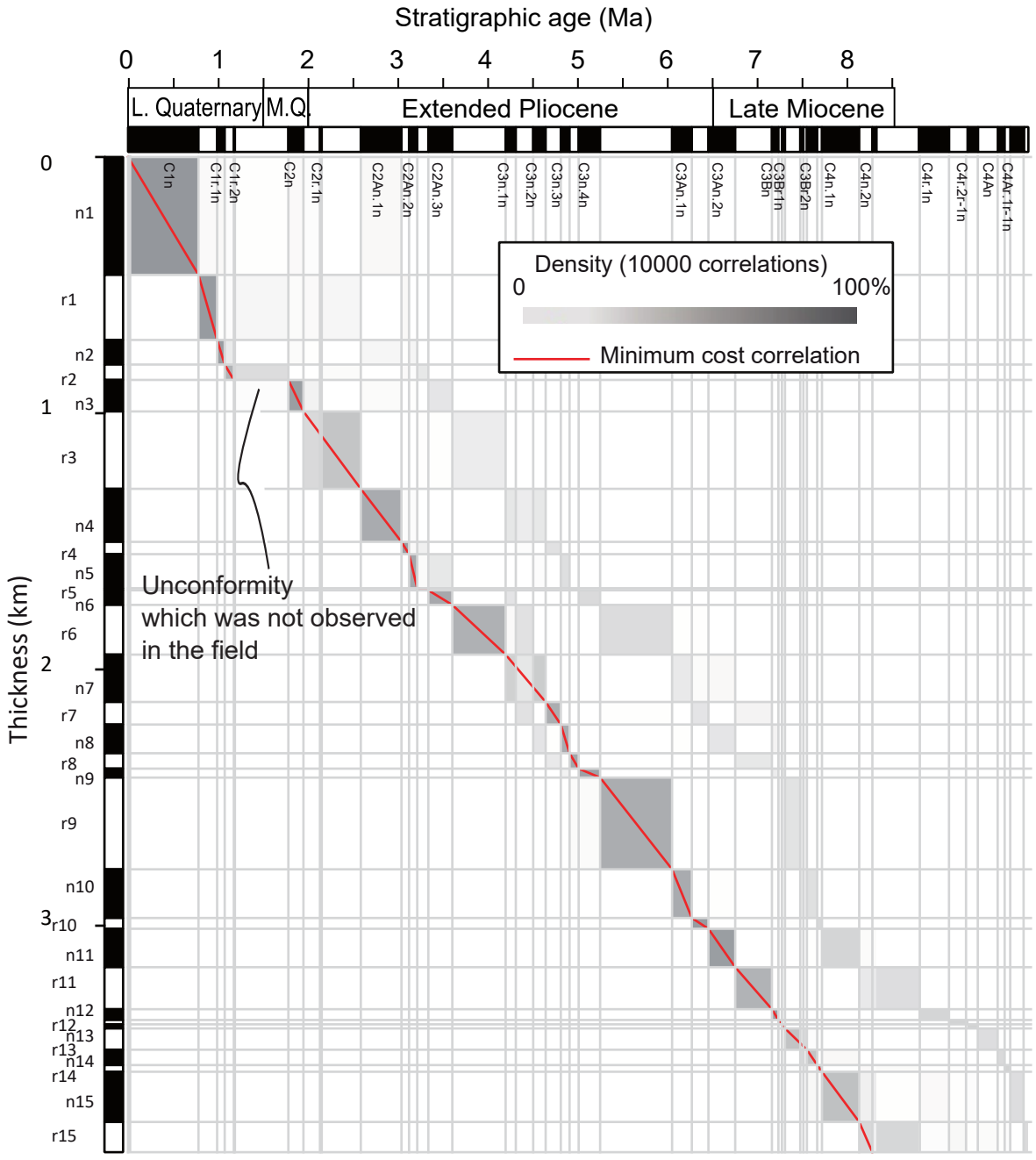

Fig. S5. Alternative magnetostratigraphic column. As in Fig. 8, composite EVF Section only with correlation to the reference scale (Ogg, 2012) using (Lallier et al., 2013). One sample shows a possible normal n2 polarity interval. But this correlation creates an unconformity that we did not observed in the field (see § 4.2.). We discarded the sample from the correlation and only retain the correlation shown Fig. 8.

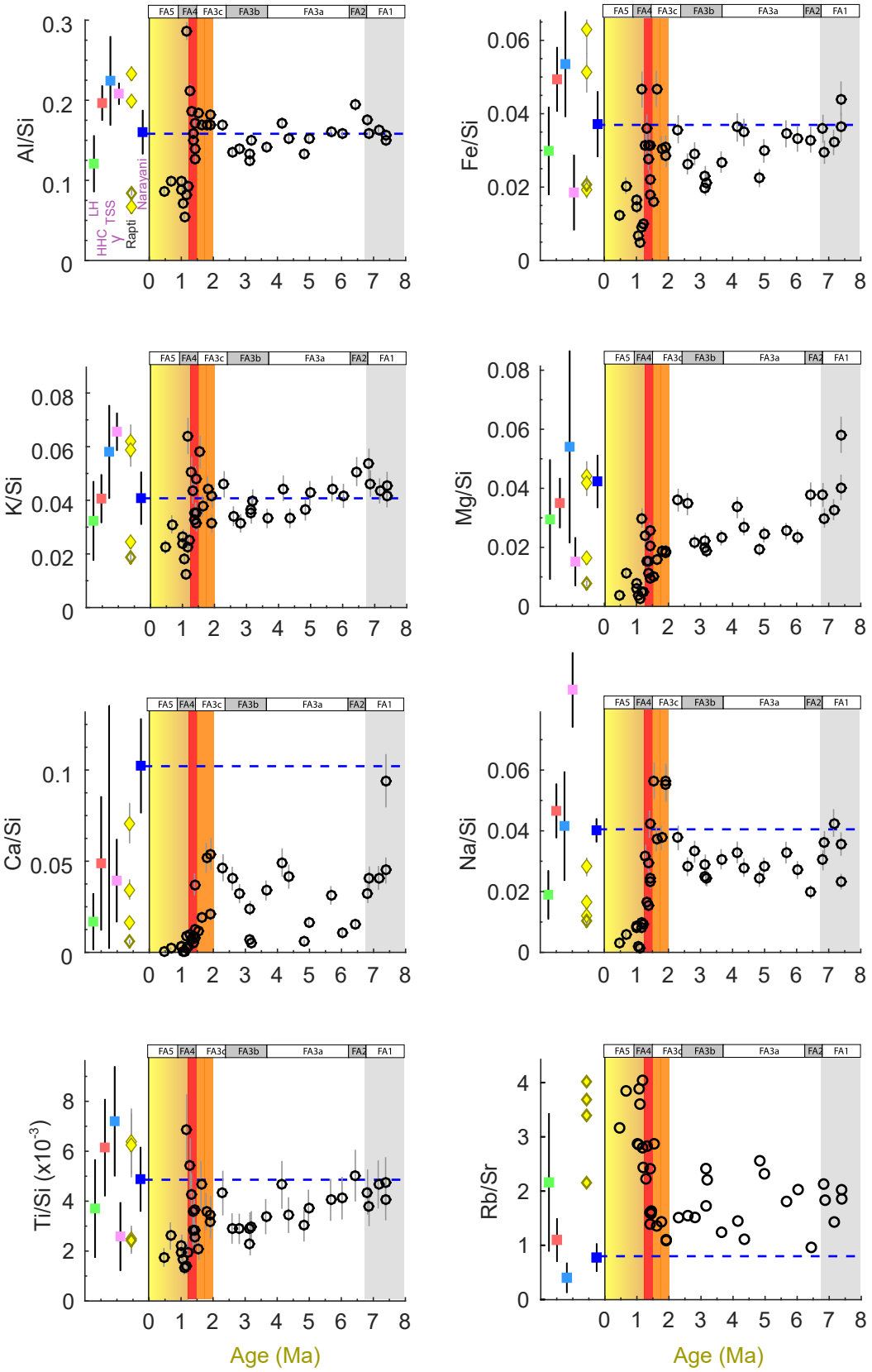

Fig. S6. Major element over time in our sandy samples. Major elements presented as ratios normalized to Si, and Rb/Sr ratio. Displayed on the left for comparison: (1) the main Himalayan geological units, the HHC, TSS, LH + the HH granites (Morin, 2015), and (2) modern sand of the Narayani River (in blue), and modern sediment of the Rapti River, this latter mostly drain in Siwalik reliefs in the Chitwan Dun. The two lowest values for Al/Si, Fe/Si or K/Si correspond to sandy deposits, whereas the two others to silty deposits or suspended load.

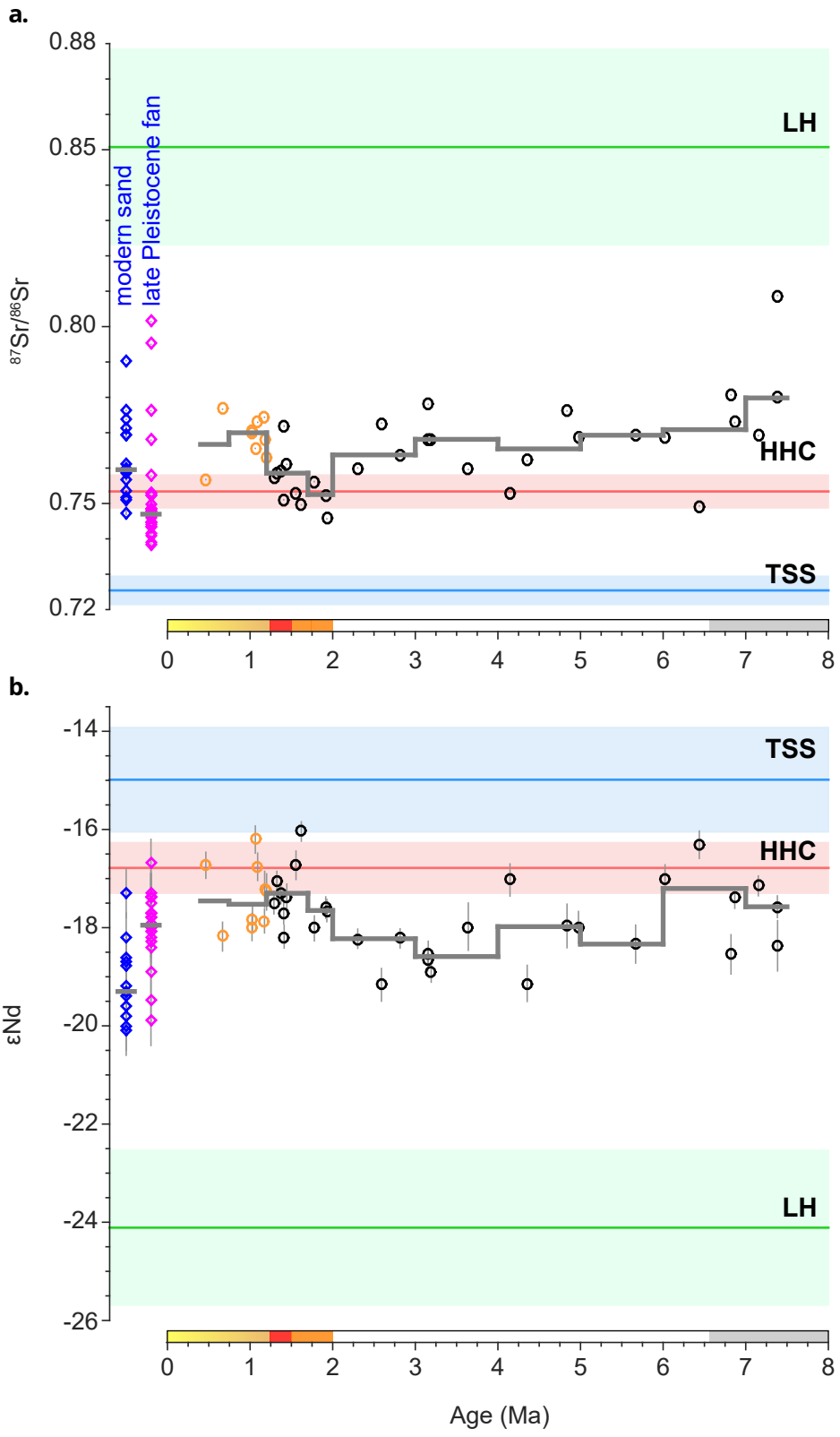

Fig. S7. Sr and Nd isotopes over time in our sandy sample. a. Black-contoured circles: 87Sr/86Sr values of the Valmiki Section. Orange-contoured circles: samples considered as recycled from Siwalik sediment. For comparison, blue- and pink-contoured diamonds: Narayani River sand and late Pleistocene Narayani Megafan (Morin, 2015). The three main units HHC, TSS and LH are indicated (Morin, 2015). b. The εNd values of the Valmiki Sections are represented similarly to a.

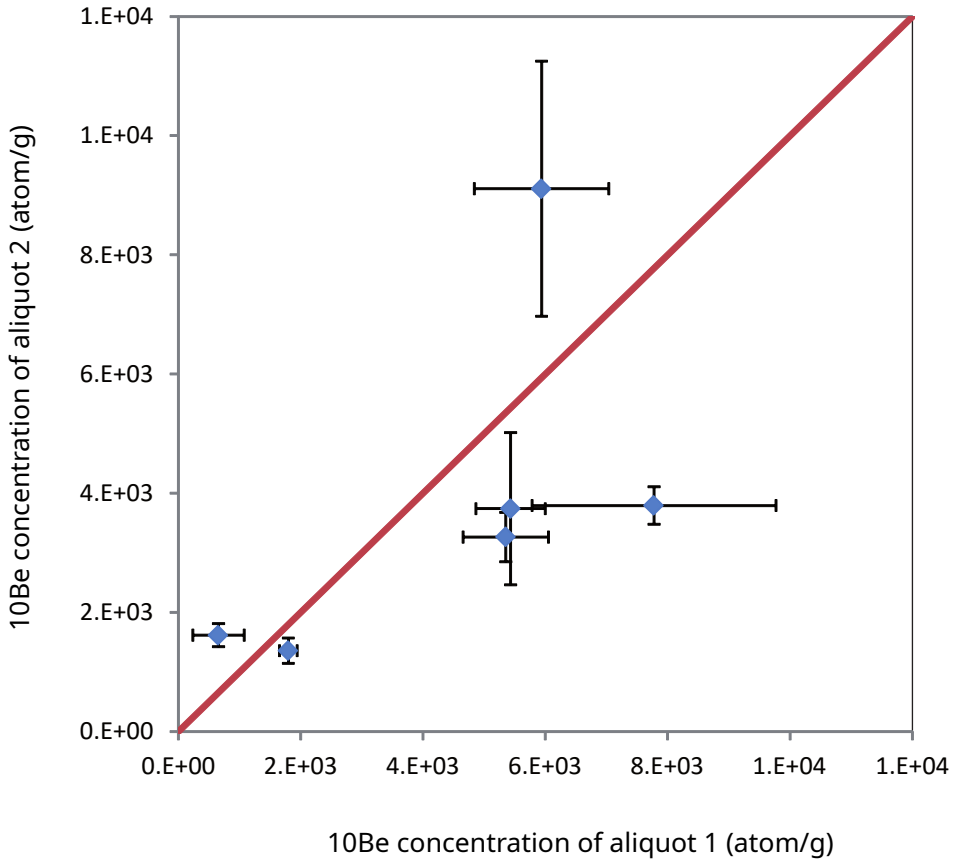

Fig. S8. Reproducibility test for the 10Be concentrations. Data from the duplicates indicated in Tab. S8.

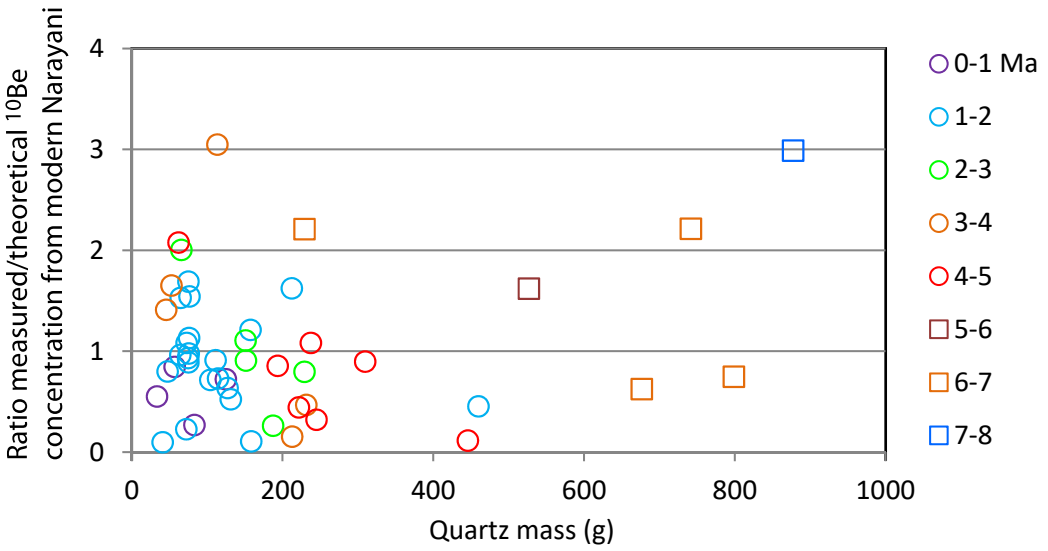

Fig. S9. Measured 10Be concentrations vs dissolved mass of quartz. To check a possible correlation of 10Be concentrations with the dissolved mass of quartz, this chart presents the ratio of measured 10Be concentrations vs concentrations expected if erosion rate is similar whatever the sample. We do not observe any correlation between ratio and mass, which might support our conservative decision to take the higher measured 9Be (see § 3.5. and Tab. S7).

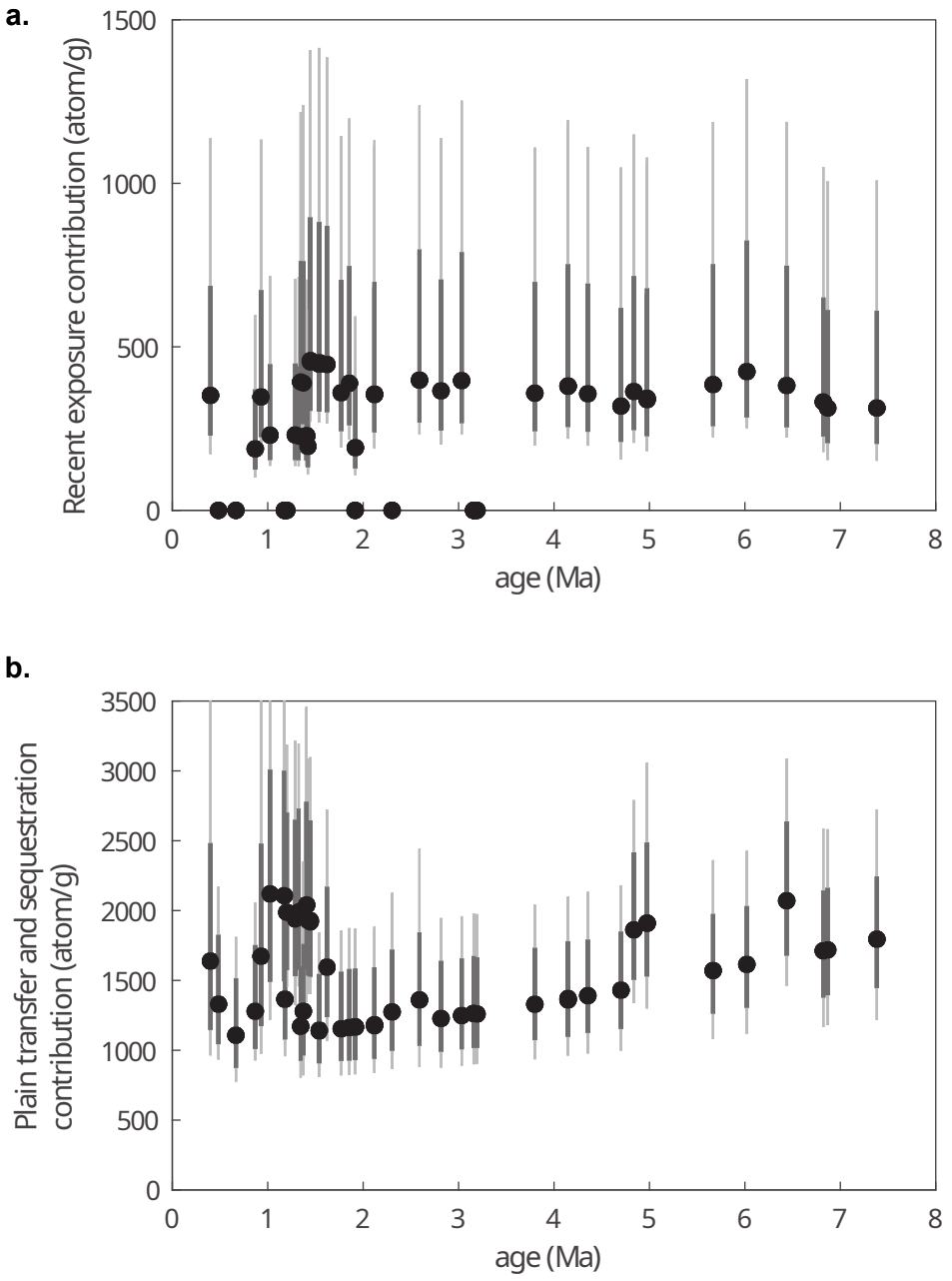

Fig. S10. 10Be corrections for recent exhumation (a) and floodplain-transfer (b) exposure. Black-filled circles: median values. Thick and thin lines: one-sigma and two-sigma error bars.

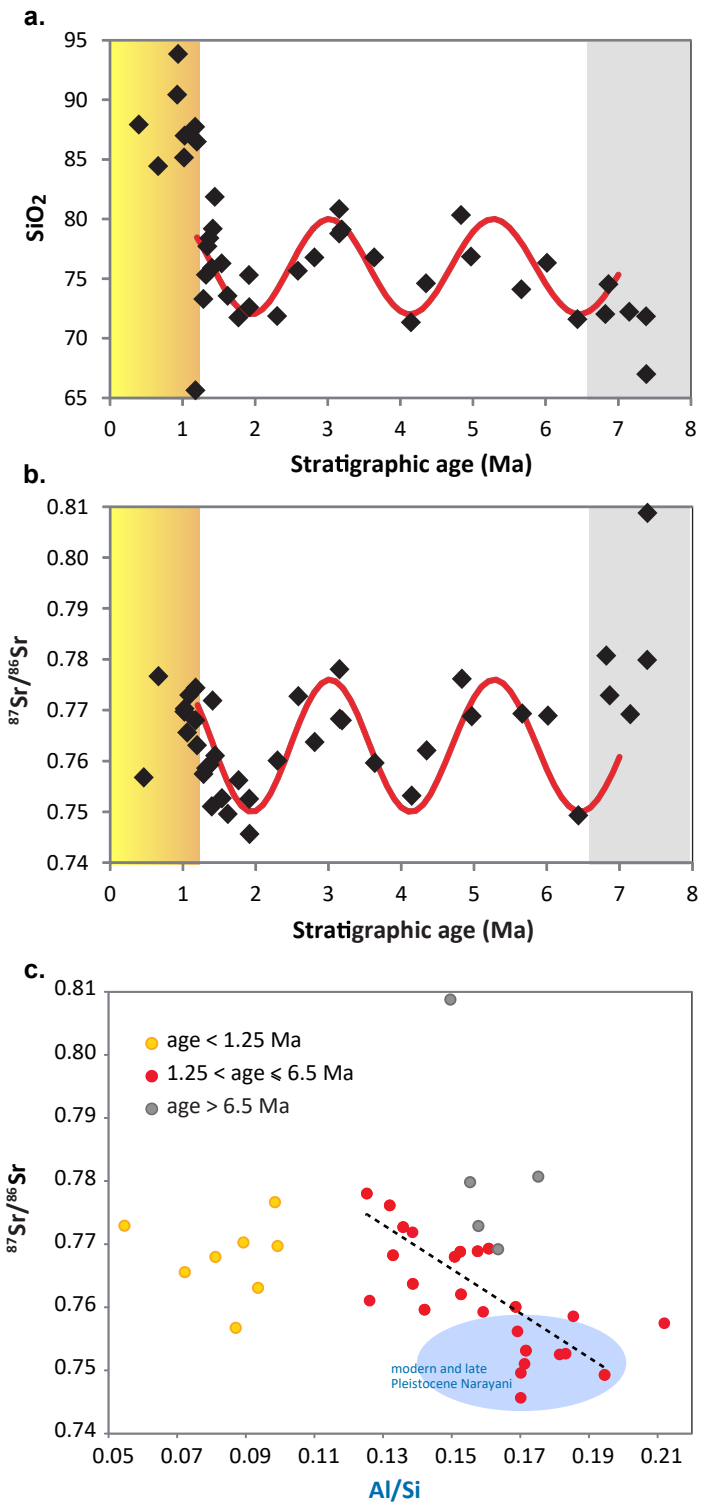

Fig. S11. (a) 87Sr/86Sr and (b) SiO2 follow similar cycles between 6.5 and 1.25 Ma. c. Samples between 1.25 and 6.5 Ma (red-filled circles) are negatively correlated to 87Sr/86Sr and Al/Si, which reflects the synchronous variations of insets a. and b. Pre-6.5 Ma samples (gray-filled circles) depart from this trend and show a more radiogenic signature for a given Al/Si ratio, whereas post-1.25 Ma recycled samples (orange-filled circles) are enriched in quartz.

S2. Supplementary table captions.
In « Supplementary Tables.xls » file attached.

Tab. S1. Measurements of bedding strike and dips, and their location along the three subsections of the composite EVF Section.

Tab. S2. Location, stratigraphic depths and ages of all collected samples from the composite EVF and WVF Sections. Type indicates whether we collected the sample for paleomagnetism (Mag), or isotopic measurements (Sandy). We calculated stratigraphic depth from tape-meter measurements and GPS coordinates. We derived ages from the magnetostratigraphic age model (see § 4.2.). Arbitrary one-sigma age uncertainty of 0.1 Ma. Note that (1) not all samples for cosmogenic measurements (i.e. below Dwcos25) were analysed in this study, (2) some samples have duplicates (e.g. T501 and T502), and some samples, without being duplicates, belong to the same strata (e.g. Dwcos8 and Dwcos44). Stratigraphic positions of sandy and paleomagnetic samples having reliable results are displayed in Fig. 8.

Tab. S3. Paleomagnetic directions. Composite EVF Section only. D: magnetic declination, I: magnetic inclination, g: geographic coordinates, s: stratigraphic coordinates, a95: radius of the fan in which the mean direction lies within 95% confidence, N: normal polarity, R: reverse polarity, Int: intermediate direction, GC: remanent direction trajectories that follow great circle paths, unstable: unstable directions, which cannot be interpreted.

Tab. S4. Major elements for our sandy samples. Elemental ratios normalized by Si. Measurement below the detection limit indicated by < D.L. Samples Ggcos1, Ggcos3, Dwcos7, Dwcos9, Dwcos13, Dwcos17, Dwcos20 without major and trace element measurement, nor Sr-Nd isotopic measurement.

Tab. S5. Trace elements for our sandy samples. Measurement below the detection limit indicated by < D.L.

Tab. S6. Sr-Nd isotopes for our sandy samples. The $^{143}Nd/^{144}Nd$ are reported as εNd(0), using CHUR(0) = 0.512638 (Goldstein et al., 1984), and relative contributions of the main geological units. The ~40% of the TSS contribution originating from carbonates is not included. Sample Dwcos32 falls outside the ternary diagram defined by the three main Himalayan lithologic unit poles (HHC, TSS and LH), so that its projection on the HHC-LH mixing curve is an approximate value.

Tab. S7. ^{10}Be blank-corrected modern concentrations. Mass of quartz decontaminated from the atmospheric contribution, with 1.5% 1-sigma uncertainty. Measurement of ^{9}Be before dissolution was calculated from the ^{9}Be carrier concentration, with 2.92% 1-sigma uncertainty. Measurement of ^{9}Be after evaporation determined by CRPG-SARM, with 12.5% 1-sigma uncertainty. The two ^{9}Be measurements are distinct, because of the potential enriched Be content due to the large mass of dissolved quartz. The ^{10}Be concentration was computed using the maximum of these two values. $^{10}Be/^{9}Be$ measured by CEREGE-ASTER. We extracted Be from samples in several series, each of them having average chemical blanks indicated here. The blank is 13% of the $^{10}Be/^{9}Be$ ratio on average (“Proportion of the correction of the blank”) and up to 52% for Dwcos8 which was analyzed in a series with a higher blank close to 10^{-14}. The ^{10}Be concentrations presented here were only corrected from the blank. Some samples are duplicates and indicated by * and **. Two sets of two samples were sampled in the same sandstone layer and indicated by # and ##. Both duplicates and samples from the same strata are pooled and averaged for paleoerosion rate calculation.

Tab. S8. ^{10}Be Himalayan paleoconcentrations and paleoerosion rates. The paleoconcentrations are corrected for recent exposure during Siwalik exhumation (C_{rex}), transfer and burial through the plain (C_{fp}), and radioactive decay. Correction for recent exposure is calculated according to ^{36}Cl calibrated model (Eq. 3 § 3.7.2.), height and approximate slope of the sampled cliff or river bank, and a qualitative coefficient for evidence of very recent erosion. Correction for transfer and burial through the plain are calculated according to the model parameters presented in Tab. S9 and to the depth of the sample below the top of the stratigraphic layer, in which we sampled. The field "Proportion of corrections" indicates which proportion of the concentration represents the transfer and exhumation corrections. The average erosion rate for duplicates (*,**) and samples taken in the same strata (#,##) is calculated from the weighed average of the paleoconcentrations. We reported for information apparent paleoerosion rates for samples younger than 1.25 Ma. However, we do not consider or discuss these rates since we presume that the sediment of these young samples is not directly issued from the erosion of the paleo-Narayani Catchment.

Tab. S9. Parameters used for the flood plain transfer model. We determined these parameters from our observations on the modern channel using satellite imagery (Google Earth©) (sinuosity including average obliquity of the river relative to a radial direction) or from published studies, 1: (Lupker et al., 2012b); 2: (Morin et al., 2018); 3: (Jain and Sinha, 2003); 4: (Dubille and Lavé, 2015); 5: (Pati et al., 2019).

Tab. S10. Feldspar fraction chemical and ^{36}Cl AMS results. All variables required for calculating a ^{36}Cl cosmogenic and radiogenic production using CREp Chlorine-36 exposure age calculator (Schimmelpfennig et al., 2022) are also provided: porosity, major and trace elements of the whole rocks, major elements and [Cl] content in the feldspars fraction. Chemical measurement below the detection limit is indicated by < D.L.

Tab. S11. Recent ^{10}Be exposure computation based on ^{36}Cl results, and steady erosion model. We determined the ^{36}Cl cosmogenic and radiogenic contributions using the CREp Chlorine-36 exposure age calculator (Schimmelpfennig et al., 2022), and the variables given in Tab. S10. For the recent exposure model, we took the outcrop-dependent parameters from Tab. S8.

S3. Extended Methods.

S3.1. Magnetostratigraphy and stochastic correlation dating.

S3.1.1. Sampling.

We sampled the Patalaia, Ganguli and Dwarda for the composite EVF Section (Fig. 3 and Tab. S1). We targeted red to brown silt in overbank deposits in the Patalaia ande Ganguli surveys, and at the top (< 750 m) and the bottom (> 2,750 m) of the Dwarda survey. In the rest of the Dwarda, we rarely collected silt and mostly fine to coarse salt and pepper sandstone. We used a gasoline-powered drill, and we oriented samples using magnetic and whenever possible, sun compasses. The average magnetic declination anomaly is of 3.4 ± 2.2° (N = 347). We prepared all cores into standard specimens of about 10 cm^3. Each sampling site has two or three cores. A 20 to 30% of samples was in loosely consolidated rocks: we housed these oriented samples in plastic boxes (8 cm^3) rather than drilling them. Horizontal spacing between two sites varies from 1 to 53 m and is 10 m on average.

S3.1.2. Magnetic mineralogy.

We investigated mineralogy with thermo-magnetic curves to determine the Curie points, Isothermal Remanent Magnetisation (IRM) and hysteresis acquisitions (Fig. S3-S4). We measured thermomagnetic curves at CRPG on porphyrized sediment, using an AGICO MFK1 Kapabridge susceptibilitymeter coupled with a CS4 furnace under argon atmosphere to avoid oxidation of magnetic minerals during heating (Fig. S3). We measured IRM acquisition curves and hysteresis loops on the same samples at IPGP on a vibrating sampler magnetometer (VSM Micromag 3900) (Fig. S4).

S3.1.3. Demagnetization and magnetic directions.

We were not able to apply stepwise thermal demagnetization because 20-30% of samples were housed in plastic cubes. Therefore, for all samples, we applied AF demagnetization at IPGP to assess the magnetic remanence. We demagnetized samples in 10 to 12 steps from 1 to 100 mT. We measured the remanent magnetization on a 2G Enterprises horizontal DC SQUID cryogenic magnetometer in the same laboratory. We identified magnetic components using stereographic projections and orthogonal vector diagrams (Zijderveld, 1967). We computed the principal component and the mean directions using Fisher statistics with the Paleomac software (Cogné, 2003; Fisher, 1953; Kirschvink, 1980).

S3.1.4. Magnetostratigraphic column and correlation to the reference scale.

We created a composite column of the EVF Section by determining the relative stratigraphic position between samples of the Patalaia, Ganguli an Dwarda based on their coordinates, strikes and dips of the bedding and bed correlation between the section using high resolution satellite imagery. We established the magnetic polarity sequence of the column based on samples with a clear, unambiguous magnetic component only. We identified magnetic intervals as at least two successive sample sites with the same polarity. We correlated the column to the reference scale of (Ogg, 2012) to determine stratigraphic ages. To minimize ambiguities and uncertainties, rather than using a manual correlation, we used a numerical method based on the dynamic time warping (DTW) algorithm (Lallier et al., 2013) and we automatically calculated 10,000 likely correlations. In this approach, the correlations are computed to minimize the local variation of the accumulation rates.

S3.2. Sr-Nd isotopic composition measurements.

We compare isotopic composition of past sediment with analog modern river sediment. This provides information to determine recycling of weathered sediment and identify potential changes in sediment

provenance. In the Himalaya, Sr and Nd isotopic analyses in past foreland sediment provide a tool to reconstruct the evolution of sediment provenance through time (Huyghe et al., 2001; Mandal et al., 2019; Robinson et al., 2001; Szulc et al., 2006).

To complement the studies that have constrained the isotopic signatures of the main Himalayan geological units (Deniel et al., 1987; France-Lanord et al., 1993; Parrish and Hodges, 1996; Robinson et al., 2001), (Morin, 2015) analyzed the sediment of rivers draining specific units, to determine the isotopic signature of those units. Their results provide a synthesis on the isotopic signature of the three main Himalayan units in Central Nepal, the HHC, TSS and LH. A low εNd between -20 and -26 and a high $^{87}Sr/^{86}Sr$ ratio characterize the LH. In contrast, the HHC and TSS have a less negative εNd between -14 and -17 and their $^{87}Sr/^{86}Sr$ ratio are ~0.76 for HHC and ~0.72 for TSS.

We prepared and measured our sandy samples for Sr-Nd isotopes at CRPG after acetic acid leaching (Hein et al., 2017). We collected bulk aliquots of the samples before the ^{10}Be sample preparation. We powdered and leached the aliquots with 10% acetic acid (Galy et al., 1996) and prepared them to obtain a silicate residue. We measured $^{87}Sr/^{86}Sr$ on the residue using a Triton Plus(TM) multi-collector thermal ionization mass spectrometer with NBS-987 as a standard and quality control. We measured $^{143}Nd/^{144}Nd$ using a Neptune plus multi-collector inductively coupled plasma mass spectrometer. We first normalized $^{143}Nd/^{144}Nd$ to $^{146}Nd/^{144}Nd = 0.7219$ using an exponential law and then to the JNdi-1 following a pseudo-standard sample-bracketing method (one standard for each 4–5 samples, Yang et al., 2017). We report the $^{143}Nd/^{144}Nd$ values as εNd(0), using CHU(0) = 0.512638 (Goldstein et al., 1984).

We compare our results (Fig. 10-11 and Tab. S6) with data from the modern Narayani sediment (Singh et al., 2008; Morin, 2015) and from cores in the late Pleistocene Narayani-Gandak Fan (Morin, 2015).

S3.3. Relative contribution of the geological units to the sedimentary mix.

We followed the approach described in Morin (2015, p. 319) to compute the fractions of TSS, HHC and LH in our sandy samples. Considering i = 1, 2 and 3 the different units and f_i their respective relative fractions, the concentration C of each isotope in the ternary mixing is defined by the equation:

$$C = \sum_{i=1}^{3} f_i \times C_i \qquad \text{(Eq. SI.1)}$$

Due to the tight range of values in isotopic compositions of Sr and Nd, ^{86}Sr and ^{144}Nd are close to a constant fraction of total [Sr] and [Nd] respectively. After combination of the respective equations for each member of the coupled isotopes (^{86}Sr and ^{87}Sr, or ^{144}Nd and ^{143}Nd), and arranging a linear relationship with respect to f_1, f_2, f_3, we obtain for the two couples of isotopes, $^{87}Sr/^{86}Sr$ or $^{143}Nd/^{144}Nd$:

$$\sum_{i=1}^{3} f_i \times C_i \times \left(R - R_i\right) = 0 \qquad \text{(Eq. SI.2)}$$

with R the isotopic ratio measured in the sediment, and R_i the isotopic ratio of each unit. We solved the set of equations with a Monte-Carlo simulation using 10,000 iterations. We set the ratios and concentrations for each unit from the mean values of (Morin, 2015). We propagated the analytical uncertainties of our isotopic measurements to examine the relative evolution of the respective fractions. For the relative contributions of the Himalayan units presented here (Fig. 11 and Tab. S6), we do not take into account the carbonate contribution, accounting for ~40% of the effective contribution of the TSS to the Narayani modern sand.

S3.5. $^{10}Be/^{9}Be$ measurement.

We prepared a total of 42 samples of fine to medium mostly unconsolidated sandstone for analyses of ^{10}Be concentrations. To limit the potential contamination by a recent exposure to cosmic rays, we selected most sampling sites in fresh exposure at the bottom of cliffs of several meters presently incised by the Siwalik rivers. Assuming that the ^{10}Be concentrations in samples were probably low because of potentially high erosion rates (> 1 mm/y), we sampled unusually large masses of sand (1 to 5 kg) to extract a sufficient amount of quartz and a measurable amount of ^{10}Be.

We prepared all samples except four at CRPG for ^{10}Be measurements following the ASTER-CEREGE procedure, similar to (Lupker et al., 2012a; Lupker et al., 2017; Puchol et al., 2017; Charreau et al., 2020), and using a sufficient amount of quartz (i.e. > 100 g, representing 10^8 to 10^{10} grains of quartz) to lower analytical uncertainties for older samples. We similarly prepared four samples at CEREGE (Aix-Marseille, France). This study focused on fractions in the 125-250 µm or 140-280 µm range of grain sizes, except for two samples. For these samples, we selected the 250-500 µm fraction either because the 125-250 µm was too small (Dwcos22) or because sample purification failed (Dwcos11). We sieved each sample under water and then carried out magnetic separation and sodium polytungstate density separation (< 2.8). We separated feldspar from quartz for ^{36}Cl measurements using flotation on a first batch of five samples, and using density separation (< 2.63) on a second batch of five samples for which we wanted to collect mostly K-feldspar. We repeated selective leaching in H_2SiF_6 and HCl to get quartz-enriched samples. For each sample, we inserted the quartz fraction in one Nalgen© bottle, except for samples of quartz mass > 260 g which we inserted in two or three bottles. We removed meteoric ^{10}Be by 3 sequential HF etchings in stoechiometric proportions to dissolve 30 wt% of the quartz in each bottle (Brown et al., 1992). We measured the remaining mass of quartz.

A small mass of a ^{9}Be carrier of known concentration was added to the quartz which was subsequently dissolved in HF. For the samples with two or three bottles, we added the carrier into one bottle only. For eight samples, we took the carrier from an industrial solution having $\left[{}^{9}Be_{carrier}\right]$ = 1,000 ppm and $\left({}^{10}Be/{}^{9}Be\right)_{carrier}$ = 1.4±0.3x10^{-15}. To measure old samples with low ^{10}Be concentrations, the carrier was made in-house from phenakyte minerals. The carrier presents $\left[{}^{9}Be_{carrier}\right]$ = 2,020±83 ppm and $\left({}^{10}Be/{}^{9}Be\right)_{carrier}$ = 4±2x10^{-16}, except for the four samples prepared at CEREGE for which the carrier presents $\left[{}^{9}Be_{carrier}\right]$ = 3,025 ppm and $\left({}^{10}Be/{}^{9}Be\right)_{carrier}$ = 1.4±0.3x10^{-15}. We evaporated the dissolved solutions in Evapoclean© 150 ml tubes at 110 °C (during several days for the oldest samples). We dissolved the residue in HCl and purified it on two successive columns per sample by anion exchange, cation exchange, alkaline precipitation, and oxidation. We note that the columns have been previously calibrated for 30-50 g of quartz by CEREGE and have not recalibrated for the large masses of quartz we used, which probably induced a low-quality purification for the oldest samples and affected the precision of our measurements. Finally, we precipitated the solution as $Be(OH)_2$ and dehydrated it to BeO at 1,000 °C.

We measured $\left(\frac{{}^{10}Be}{{}^{9}Be}\right)_{quartz}$ on the BeO target at ASTER-CEREGE (Arnold et al., 2010), with a normalization to the in-house standard STD-11, using an assigned ^{10}Be/^{9}Be ratio of (1.191 ± 0.013) x 10^{-11} (Braucher et al., 2015). We separated ten procedural chemical blanks and measured them using a similar procedure, obtaining an average $\left(\frac{{}^{10}Be}{{}^{9}Be}\right)_{blank}$ = 10^{-14} for the industrial carrier and 3x10^{-15} for the in-house carrier. Our results are presented in Tab. S7.

S3.6. ^{10}Be concentration determination.

We performed a check on potential natural ^{9}Be content in the quartz that could interfere with the ^{9}Be content of the carrier (see discussion in (Lupker et al., 2017)). After evaporation and dissolution in HCl, we collected an aliquot for ^{9}Be measurement using ICP-MS at CRPG. As in a previous study (Lenard et al., 2020), we expected that the measured concentrations be slightly lower than the predicted concentrations ("^{9}Be added before dissolution" and "^{9}Be measured after evaporation" columns in Tab. S7), because of the potential loss of Be after addition of the ^{9}Be carrier, during dissolution and evaporation. However, for the majority of samples, we found ^{9}Be concentrations 0-60% higher than the ^{9}Be concentrations predicted from the added mass of the carrier, with levels > 100% for some samples with a large mass. This might suggest that natural ^{9}Be content is not negligible for the Valmiki samples, as for the Bhutanese river sand (Portenga et al., 2015).

For the computation of ^{10}Be concentrations ("^{10}Be blank-corrected modern concentrations" in Tab. S7), we conservatively considered the higher ^{9}Be content from the predicted and measured contents. For the samples without ^{9}Be measurement, we applied a 1-sigma uncertainty of 25% on the ^{9}Be concentration.

Our results in Tab. S7 (before plain exposure and recent exposure corrections) and Tab. S8 (these corrections included) are compared with published ^{10}Be data obtained from modern Narayani sand, 125-250 μm fractions collected at Narayangarh, Nepal and obtained with methods similar to ours (Lupker et al., 2012a).

S3.7. ^{10}Be correction for exhumation from ^{36}Cl measurement.

S3.7.1. ^{36}Cl measurement.

The recent Siwalik exhumation has exposed our sampled outcrops to cosmic rays. This affects the original ^{10}Be concentrations and requires correction. Due to the rapid radioactive decay of the ^{36}Cl, ^{36}Cl paleoconcentrations inherited from Himalayan erosion fall to negligible values after ~2 My. Therefore for older samples, any ^{36}Cl content in the feldspar of our samples results from recent exposure. The ^{36}Cl measurement in the feldspar of our sample provides a simple way to assess the ^{10}Be contribution of recent exhumation.

We prepared the feldspar fraction of five samples for ^{36}Cl extraction at CEREGE following the protocol of (Schimmelpfennig et al., 2011). We washed the samples with milliQ water and etched them in limited amounts of a mixture of HF (40%)/ HNO_3 (10%) (volume ratio 1:2) to dissolve ~10% mass. We took a 1-g aliquot for chemical composition measurement at SARM-CRPG. We added ~1.9 mg of chloride in the form of a chloride carrier enriched in ^{35}Cl (99.9%), to the samples. We dissolved the samples with an excess amount of the HF/HNO_3 mixture. We separated the supernatant by centrifuging from the fluoric cake formed during the dissolution reaction. We precipitated AgCl by adding $AgNO_3$, redissolved it in dilute NH_4OH, and added $Ba(NO_3)_2$ to precipitate $BaSO_4/BaCO_3$, in order to lower the isobaric interference of ^{36}S during ^{36}Cl AMS measurement. We precipitated AgCl with HNO_3 and collected the precipitate by centrifuging. We rinsed and dried the AgCl precipitates.

We determined $^{36}Cl/^{35}Cl$ and $^{35}Cl/^{37}Cl$ from isotope dilution AMS measurement at ASTER-CEREGE, normalized the ratios to a ^{36}Cl standard prepared by K. Nishiizumi (Sharma et al., 1990), The $^{36}Cl/^{35}Cl$ ratios of the first batch were normalized to a ^{36}Cl standard prepared by K. Nishiizumi (Sharma et al., 1990), while that of the second batch was normalized to the in-house standard SM-CL-12 (Merchel et al., 2011), in both cases assuming a natural $^{35}Cl/^{37}Cl$ ratio of 3.127. We carried out chemical measurement in feldspar at SARM. The results are presented in Tab. S10.

To calculate the contributions to ^{36}Cl production through the radiogenic and cosmogenic pathways (spallation, muon and low-energy neutron capture), we used the CREp Chlorine-36 exposure age calculator (Schimmelpfennig et al., 2022) in its spreadsheet version (Schimmelpfennig et al., 2009) to be able to estimate the contributions from the radiogenic and various cosmogenic ^{36}Cl production reactions and to handle the overestimated radiogenic ^{36}Cl contributions leading to negative age and cosmogenic component values in a few

samples. We calculated ^{36}Cl production rates for the radiogenic and cosmogenic components assuming that the sandy samples were saturated with water during most of their burial. We first assessed the porosity p (in %) based on sample stratigraphic depth z (in m) and using the following empirical relationship:

$$p = 42 \pm 5 \times e^{\frac{-z}{3700}}, \quad \text{(Eq. SI.3)}$$

based on (Baldwin and Butler, 1985) formula for sandstone, adjusted to porosity measurement in the Siwalik sandstone of Central Nepal (Dubille, 2008). We then normalized the element content of the sample to the total mass of the rock, including water in pore space. This normalization substantially reduces the radiogenic ^{36}Cl production component by 'diluting' the U, Th content and thus the thermal neutron production related to the radioactive decay of U and Th, and by modulating the cosmogenic epithermal and thermal neutron fluxes due to hydrogen moderating the neutron energies.

S3.7.2. Estimation of the ^{10}Be correction for exhumation from ^{36}Cl measurement.

For samples older than 2 Ma, we applied (Eq. 2) to assess the ^{10}Be component due to recent exhumation. For samples younger than 2 Ma, due to insufficient radioactive decay, we cannot neglect the initial $^{36}Cl_{paleo}$ before sediment burial, compared with the recent exposure component. In that case, for ^{36}Cl and ^{10}Be, we write:

$$^{10}C = {}^{10}C_{paleo} \cdot e^{-\lambda_{10} t} + {}^{10}C_{rex} \quad \text{(Eq. SI.4)}$$

$$^{36}_{cosmo}C = {}^{36}_{cosmo}C_{paleo} \cdot e^{-\lambda_{36} t} + {}^{36}_{cosmo}C_{rex} \quad \text{(Eq. SI.5)}$$

with λ_{36} and λ_{10} the radioactive decay constants of ^{36}Cl and ^{10}Be, respectively, and t the stratigraphic age of our samples.

Assuming that (1) feldspar and quartz are distributed similarly in the Narayani Catchment, and that (2) the production ratio $K_{\frac{10}{36}} = P_{Q\_10}/P_{F\_36}$ in Himalayan and Siwalik outcrop rocks at erosion are roughly similar:

$$^{10}C_{rex} = K_{10/36} \cdot {}^{36}_{cosmo}C_{rex} \quad \text{(Eq. SI.6)}$$

and $$^{10}C_{paleo} = K_{10/36} \cdot {}^{36}_{cosmo}C_{paleo} \quad \text{(Eq. SI.7)}$$

For rocks exhumed steadily, $K_{\frac{10}{36}}$ roughly simplifies as:

$$K_{\frac{10}{36}} = \frac{P_{Q\_10}}{P_{F\_36}} = \frac{\sum_{j=1,2,3} \Lambda_j \cdot {}_{10}P_j}{\sum_{j=1,2,3} \Lambda_j \cdot {}_{36}P_j} \quad \text{(Eq. SI.8)}$$

with P_j the local cosmogenic production rate at given elevation and latitude for all pathways (spallation, slow and fast muon for ^{10}Be; spallation, slow muon, thermal and epithermal neutron for ^{36}Cl), and with Λ_j the attenuation lengths for the pathways (g.cm^{-2}).

We note that the relative contributions of muons, thermal and epithermal neutrons to spallation vary with elevation, and that Himalayan lithologies may have variations in relative feldspar/quartz content. However, we assume that this does not alter $K_{\frac{10}{36}}$ by more than ~20 % between the Middle Narayani Catchment and the Valmiki Section.

Combining (Eq. SI.5) and (Eq. SI.7) into (Eq. SI.4) to suppress the paleo-components gives

$$^{10}C = K_{\frac{10}{36}} \cdot \left({}^{36}_{cosmo}C - {}^{36}_{cosmo}C_{rex} \right) \cdot e^{\left(\lambda_{36} - \lambda_{10}\right) \cdot t} + {}^{10}C_{rex} \quad \text{(Eq. SI.9)}$$

And then $^{10}C = K_{\frac{10}{36}} \cdot {}^{36}_{cosmo}C \cdot e^{(\lambda_{36}-\lambda_{10}).t} + {}^{10}C_{rex} \cdot \left(1 - e^{(\lambda_{36}-\lambda_{10}).t}\right)$ (Eq. SI.10)

At first order, we finally estimate the recent ^{10}Be and $^{36}Cl_{cosmo}$ exposure contribution with:

$$^{10}C_{rex} = \frac{\left({}^{10}C - {}^{36}_{cosmo}C \cdot K_{\frac{10}{36}} \cdot e^{(\lambda_{36}-\lambda_{10}).t}\right)}{\left(1 - e^{(\lambda_{36}-\lambda_{10}).t}\right)} \quad \text{(Eq. SI.11a)}$$

and

$$^{36}_{cosmo}C_{rex} = \frac{\left({}^{36}_{cosmo}C \cdot \frac{^{10}C}{K_{\frac{10}{36}}} \cdot e^{(\lambda_{10}-\lambda_{36}).t}\right)}{\left(1 - e^{(\lambda_{10}-\lambda_{36}).t}\right)} \quad \text{(Eq. SI.11b).}$$

S3.8. ^{10}Be correction for sediment transfer.

Exposure during sediment transport and burial affects the original ^{10}Be concentrations and requires a correction. To assess the ^{10}Be contribution during floodplain transfer and final burial, we used the steady state and sediment mass-balance-based model of (Lauer and Willenbring, 2010). As input parameters of the model, we used the geomorphologic parameters of the Narayani River reported in Tab. S9. We derived the parameters from published studies or from our own measurements. We derived the sediment aggradation rate from our magnetostratigraphic results and the channel lateral migration rate and sinuosity from the channel location observed over two decades of satellite imagery, available on Google Earth©.

In this model, sediment is carried into the floodplain with an initial concentration $C_c(0)$. While moving downstream, a fraction of sediment is deposited throughout reservoirs in the floodplain and replaced with sediment previously stored in these reservoirs. Each reservoir is assumed to be well-mixed off.

At a distance x measured down the channel axis from the range outlet, (Eq. 17) in (Lauer and Willenbring, 2010) yields the average ^{10}Be concentration in river sediment $C_c(x)$. In (Charreau et al., 2020), in absence of details on the sample depth within its sedimentary unit, a mean concentration in the floodplain (Eq. 6 in (Lauer and Willenbring, 2010)) was considered. In this study, we rather explicitly determined the ^{10}Be contribution once the sediment is deposited in its sedimentary unit for each sample. We considered that each sedimentary unit is deposited in a short period, one flood to a few monsoon seasons, except for multistoried thick sandstone. The depth at which the sample is in this sedimentary unit corresponds to the depth at which it begins to accumulate ^{10}Be, before being buried under the next sedimentary unit that aggrades at a 0.5 mm/y mean rate.

The mean concentration gain $C_{fp}(x)$ in the floodplain is:

$$C_{fp}(x) \cong C_c(x) - C_0 + \sum_{j=1}^{3} \frac{P_j \Lambda_j}{\sigma \rho_s} e^{\frac{-\rho_s}{\Lambda_j} min(\delta, H)} \quad \text{(Eq. SI.12)}$$

with C_0 the initial concentration at the range outlet, $C_c(x)$ the concentration of the sediment in the river at a distance x from the front, H the average bankfull depth of the Narayani River, σ the mean aggradation rate in the floodplain, P_j the production rates and Λ_j the attenuation lengths of the nucleogenic or muonic production pathways (j for spallation, slow and fast muon), ρ_s the sediment density. This equation, as other equations in this study relating ^{36}Cl and ^{10}Be concentration and erosion rate, is valid if we neglect radioactive decay, that is as long

as $\frac{\sigma \rho_s}{\Lambda_j} \gg \lambda$. In case of a thick multistoried sandstone layer, the initial deposition depth is given by the Narayani channel depth, that is its maximum possible value. We estimated the paleoposition x of the samples using their stratigraphic ages, based on a southward migration rate of the range outlet of 15±5 mm/y (Lyon-Caen and Molnar, 1985).

We computed the floodplain exposure contribution under several assumptions that do not impact the order of magnitude of our results: (1) the active floodplain depth, (2) aggradation rate, (3) sinuosity and (4) channel lateral migration rate were considered spatially uniform from the range outlet to the floodplain outlet (Lauer and Willenbring, 2010; Lupker et al., 2012a) and (5) downstream sediment fining is also omitted.

The results of the contribution of the floodplain exposure for each sample are reported in Tab. S8.

Supplementary references.

Brown, E. T., Brook, E. J., Raisbeck, G. M., Yiou, F., Kurz, M. D. (1992). Effective attenuation lengths of cosmic rays producing 10Be and 26Al in quartz: Implications for exposure age dating. Geophysical Research Letters, 19(4), 369-372. https://doi.org/10.1029/92gl00266

Cogné, J. P. (2003). PaleoMac: a Macintosh™ application for treating paleomagnetic data and making plate reconstructions. Geochemistry, Geophysics, Geosystems, 4(1). https://doi.org/10.1029/2001gc000227

Deniel, C., Vidal, P., Fernandez, A., Le Fort, P., Peucat, J. J. (1987). Isotopic study of the Manaslu granite (Himalaya, Nepal): inferences on the age and source of Himalayan leucogranites. Contributions to Mineralogy and Petrology, 96(1), 78-92. https://doi.org/10.1007/bf00375529

France-Lanord, C., Derry, L., Michard, A. (1993). Evolution of the Himalaya since Miocene time: isotopic and sedimentological evidence from the Bengal Fan. Geological Society, London, Special Publications, 74(1), 603-621. https://doi.org/10.1144/gsl.sp.1993.074.01.40

Galy, A., France-Lanord, C., Derry, L. A. (1996). The Late Oligocene-Early Miocene Himalayan belt constraints deduced from isotopic compositions of Early Miocene turbidites in the Bengal Fan. Tectonophysics, 260(1-3), 109-118. https://doi.org/10.1016/0040-1951(96)00079-0

Goldstein, S.L., O'nions, R.K., Hamilton, P.J. (1984). A Sm-Nd isotopic study of atmospheric dusts and particulates from major river systems. Earth and planetary Science letters 70, 221-236. https://doi.org/10.1016/0012-821x(84)90007-4

Kirschvink, J. (1980). The least-squares line and plane and the analysis of palaeomagnetic data. Geophysical Journal International, 62(3), 699-718. https://doi.org/10.1111/j.1365-246x.1980.tb02601.x

Lupker, M., Lavé, J., France-Lanord, C., Christl, M., Bourlès, D., Carcaillet, J., Maden, C., Wieler, R., Rahman, M., Bezbaruah, D., Xiaohan, L. (2017). 10Be systematics in the Tsangpo-Brahmaputra catchment: the cosmogenic nuclide legacy of the eastern Himalayan syntaxis. Earth Surface Dynamics, 5(3), 429-449. https://doi.org/10.5194/esurf-5-429-2017

Lupker, M., Lavé, J., France-Lanord, C., Christl, M., Bourlès, D., Carcaillet, J., Maden, C., Wieler, R., Rahman, M., Bezbaruah, D., Xiaohan, L. (2017). 10Be systematics in the Tsangpo-Brahmaputra catchment: the cosmogenic nuclide legacy of the eastern Himalayan syntaxis. Earth Surface Dynamics 5, 429-449. https://doi.org/10.5194/esurf-5-429-2017

Mandal, S.K., Scherler, D., Romer, R.L., Burg, J.-P., Guillong, M., Schleicher, A.M. (2019). Multiproxy Isotopic and Geochemical Analysis of the Siwalik Sediments in NW India: Implication for the Late Cenozoic Tectonic Evolution of the Himalaya. Tectonics 38, 120–143. https://doi.org/10.1029/2018TC005200

Merchel, S., Bremser, W., Alfimov, V., Arnold, M., Aumaître, G., Benedetti, L., Bourlès, D.L., Caffee, M., Fifield, L.K., Finkel, R.C., Freeman, S. P. H. T., Martschini, M., Matsushi, Y., Rood, D. H., Sasa, K., Steier, P., T. Takahashi, T., M. Tamari, M., Tims, S. G., Tosaki, Y., Wilcken, K. M.,, Xu, S. (2011). Ultra-trace analysis of 36 Cl by accelerator mass spectrometry: an interlaboratory study. Analytical and bioanalytical chemistry, 400, 3125-3132. https://doi.org/10.1007/s00216-011-4979-2

Parrish, R.R., Hodges, V. (1996). Isotopic constraints on the age and provenance of the Lesser and Greater Himalayan sequences, Nepalese Himalaya. Geological Society of America Bulletin 108, 904-911. https://doi.org/10.1130/0016- 7606(1996)108<0904:ICOTAA>2.3.CO;2

Portenga, E. W., Bierman, P. R., Duncan, C., Corbett, L. B., Kehrwald, N. M., Rood, D. H. (2015). Erosion rates of the Bhutanese Himalaya determined using in situ-produced 10Be. Geomorphology, 233, 112-126. https://doi.org/10.1016/j.geomorph.2014.09.027

Robinson, D.M., DeCelles, P.G., Patchett, P.J., Garzione, C.N. (2001). The kinematic evolution of the Nepalese Himalaya interpreted from Nd isotopes. Earth and Planetary Science Letters 192, 507-521. https://doi.org/10.1016/S0012-821X(01)00451-4

Schimmelpfennig, I., Benedetti, L., Finkel, R., Pik, R., Blard, P. H., Bourlès, D., Burnard, P., Williams, A. (2009). Sources of in-situ 36Cl in basaltic rocks. Implications for calibration of production rates. Quaternary Geochronology, 4(6), 441-461. https://doi.org/10.1016/j.quageo.2009.06.003

Szulc, A. G., Najman, Y., Sinclair, H. D., Pringle, M., Bickle, M., Chapman, H., Garzanti, E., Andò, S., Huyghe, P., Mugnier, J-L., Ojha, T., DeCelles, P. (2006). Tectonic evolution of the Himalaya constrained by detrital 40Ar–39Ar, Sm–Nd and petrographic data from the Siwalik foreland basin succession, SW Nepal. Basin Research, 18(4), 375-391. https://doi.org/10.1111/j.1365-2117.2006.00307.x